Electron-phonon coupling in Ni^{2+}-doped perovskites: $KMgF_3$ and $BaLiF_3$

M. Mortier,[1] B. Piriou,[2] J. Y. Buzaré,[3] M. Rousseau,[3] and J. Y. Gesland[3]
[1]*CNRS-UMR7574, 1, place Aristide Briand, 92190 Meudon, France*
[2]*CNRS-UMR8580, Ecole Centrale de Paris, Grande Voie des Vignes, 92290 Chatenay Malabry, France*
[3]*CNRS-UMR6087, Université du Maine, Avenue Olivier Messiaen, 72085 Le Mans CEDEX 9, France*
(Received 29 April 2002; revised manucript received 21 October 2002; published 27 March 2003)

Electron-phonon (*e*-ph) coupling has been studied in two Ni^{2+}-doped fluoride crystals: the classical $KMgF_3$ perovskite and the inverted perovskite $BaLiF_3$. The purely linear character of the EP coupling is shown through the comparison of emission or excitation vibronic spectra arising from different electronic levels at low temperature and the thermal evolution of the spectra. The $[NiF_6]^{4-}$ complex is described by using the molecular orbital formalism, and its covalency is estimated from the parameters of the super hyperfine structure observed in electron spin resonance measurements. A modified Pryce model is used to simulate the vibronic band shapes of Ni^{2+} ions in the compounds from their measured phonon density of states and to estimate the Huang-Rhys *S* parameter. The strength of the crystal field and the strength of the *e*-ph coupling experienced by the Ni^{2+} ions is shown to increase with the covalency of the bonding. No effect on *e*-ph coupling has been observed when the concentration of doping ions has been increased.

DOI: 10.1103/PhysRevB.67.115126 PACS number(s): 63.20.Kr, 78.20.−e, 76.30.−v

I. INTRODUCTION

The electron-phonon (*e*-ph) coupling is the interaction between electronic transitions of optically active impurities and vibration modes of their host lattice, i.e., phonons, localized or resonant modes.[1] It is responsible for the wide absorption or emission bands of the $3d$ transition-metal ions and then for their optical properties when it gives rise to any or weak sidebands in less coupled systems such as $4f$ elements.

Though it has been extensively studied,[2–18] the *e*-ph coupling is still a matter of debate. For instance, the purely linear character of *e*-ph coupling is assumed in many discussions or simulations[6,11] and in the Pryce model[5] but it is not demonstrated when it is generally supposed to contain simultaneously linear and quadratic effects.[15]

The Born-Oppenheimer adiabatic approximation allows decoupling of electronic and nuclear displacements in the treatment of the vibronic states of an impurity, giving rise to two separated Schrödinger equations. The electronic energy eigenvalues $W_l(\mathbf{R})$, arising from the first equation, act as an effective potential for the motion of the nucleus described in the second equation. In the harmonic approximation, this potential can be expanded in a Taylor series around the equilibrium position $\mathbf{R}_{0l}$: $W_l(\mathbf{R}) = W_l(\mathbf{R}_{0l}) + a_l(\mathbf{R}-\mathbf{R}_{0l}) + b_l(\mathbf{R}-\mathbf{R}_{0l})^2$, where a_l and b_l depend on the electronic state. The b_l parameters are connected to the force constants that appear in the dynamical matrix of the crystal and determine the quadratic part of the coupling. If b_l is assumed to be independent of the electronic state, the curvature of the parabolas is the same, and we are in the linear coupling approximation. The a_l parameter determines the linear term of coupling of the *l* electronic state with the crystal vibration and thus the displacement of the parabolas.[2]

In the framework of the purely linear coupling approximation, the atomic force constants are supposed to be insensitive to the electronic transition undergone by the emitting centers. The phonon spectrum of the matrix remains unaffected when the electronic states of the doping ions embedded into the crystal are changed. In such an approximation, we neglect the effect produced on the atomic force constants by the variation of the ionic radius of the emitting ion when its electronic state changes. The effective ionic radius of the impurity is modified, increased or decreased, in an excited state, and the neighboring ions in the lattice are pushed out relative to their equilibrium position in the ground state. The ionic displacement is maximum for the nearest neighbors in the lattice and decreases rapidly with increasing distance from defect. The deviations are typically several percents of the lattice spacing for nearest neighbors in the case of localized electronic systems such as $3d$ ions or *F* centers.[5]

The phonon densities of states determined in lattice dynamical studies[19,20] correspond to undoped crystals or to doped crystals with nonexcited electronic defaults. When the optical absorption from the ground state up to excited states or the emission between two excited levels are studied, the phonon spectrum involved in the vibronic transition, which corresponds to the final electronic level, is that of an excited electronic state. In the case of an emission down to the ground level, the phonons involved in the vibronic transition correspond to the ''nonexcited'' density of states. So when the vibronic spectra associated with the different cases of electronic transitions are compared, the lattice vibration spectra associated with different electronic levels are considered and the linearity of the electron-phonon coupling can be checked. All these spectra must be recorded at low temperature, typically lower than 20 K, in order to avoid a thermal population of the phonon levels in the starting electronic level. Indeed, at higher temperatures, anti-Stokes processes are allowed by thermal populating in the initial electronic level, inducing a homogeneous broadening of the whole spectra and smoothing all their features, preventing any comparison of the phonon frequencies from spectra.

In other respects, the strength of the *e*-ph coupling for $3d$ ions has been assumed to vary with the concentration in active ions by some authors,[7–9] when other authors have shown that the coupling remained unaffected by the concen-

tration value without any pair effect.[13] This last question has also been treated in the case of $4f^n \rightarrow 4f^n$ transitions of the lanthanides even though their electronic configurations offer a very different situation.[10,14] It has also been found that, in the case of Cr^{3+}-doped oxide host lattices, the *e*-ph coupling can be dependent on the covalency of the host lattice.[12]

The aim of this paper is to give an experimental and somewhat different insight into the nature of the coupling: its linearity, the concentration dependence of its strength, and the effect of the covalency of the host crystal. In this framework, Ni^{2+}-doped perovskites $KMgF_3$ and $BaLiF_3$ have been studied.

In the cubic perovskites $KMgF_3$ and $BaLiF_3$, the Ni^{2+} ions occupy the Mg^{2+} site at the center of the fluorine octahedron in $KMgF_3$ and substitute for Li^+ ions in the inverted $BaLiF_3$ perovskite.[11,21] A charge compensation mechanism is then induced in $BaLiF_3$. But as observed by electron spin resonance (ESR) the next-nearest neighbors are not involved in this mechanism, and the local symmetry of the Ni^{2+} site remains cubic in $KMgF_3$ and $BaLiF_3$.[11,21] Time-resolved spectroscopy has been used on Ni^{2+}-doped compounds without any indication of a time-dependent effect. One unique spectrum has been attributed to Ni^{2+} ions in the different samples.

The energy-level structure of d^n and f^n ions in crystals can be explained, to a large extent, by crystal-field theory. This theory is based on the hypothesis that a magnetic ion in a crystal site ''feels'' the influence of the ligand ions as an electric field that has the symmetry of the site. In this hypothesis, no overlapping of the wave functions of the magnetic ion and of the ligands is allowed and the bonding is considered to be of pure ionic type.[22] However, the observation of a transferred hyperfine structure in the ESR spectrum for such ions reflects the mixing of the orbitals of the ion with those of the ligands, i.e., the covalent character of the bonding in fluoride perovskites.

Some spectral parameters, such as Racah's *B* and *C* and the spin-orbit interaction, are expected to be smaller in the solids than in the free ions due to covalency reduction.[22] The stronger overlap between the wave functions of the metal and the ligands must also give rise to a stronger coupling between electronic transitions of the metal and vibrations involving at least the ligands.[12] For these reasons, we first measure the covalent character of the chemical bonding in the studied crystals.

II. EXPERIMENT

A $KMgF_3$ single crystal doped with 1 mol % of $KNiF_3$ was grown using Bridgman method.[11,23] $BaLiF_3$ single crystals were grown by the Czochralski technique[24,25] doped with 0.5 or 6 mol % of Ni ions in the melt. The real concentration was determined by the inductively coupled plasma (ICP) analytical technique to be, respectively, 0.2% and 1.65% of Li substituted in the crystal.[24]

The emission measurements were achieved after excitation by the 457.9-nm line of an argon-ion laser Innova 90 (Coherent) used in the light regulation mode. The detector was a Hamamatsu R928 photomultiplier placed at the exit slit of a Coderg double-monochromator spectrometer. The mean resolution was 3 cm^{-1}. A He closed-cycle Leybold cryogenerator was used to obtain low-temperature measurements down to 10 K.

The excitation spectra were recorded using a dye laser (Coumarine 460) excited by 8-ns pulses of a frequency-tripled Nd-doped yttrium aluminum garnet (Nd:YAG) laser. The spectral resolution was better than 4 cm^{-1}. Lifetimes were measured with the R928 photomultiplier after excitation by the dye laser.

III. ESTIMATION OF THE COVALENCY OF THE $[NiF_6]^{4-}$ COMPLEX

The ground state of Ni^{2+} is the orbital singlet $^3A_2$ $(t_{2g}^6 e_g^2)$ with a spin $S=1$. In this case, two e_g electrons give rise to a non-negligible overlap with the neighboring fluorine ions of the octahedron. The monoelectronic Hamiltonian corresponding to the interaction between the *k* electron and the nuclear spin of the α fluorine may be written

$$H(\mathbf{s}_k,\mathbf{I}_\alpha)=g_e\beta_e g_N\beta_N\left\{\frac{8\pi}{3}\delta(r_{k\alpha})\mathbf{s}_k\cdot\mathbf{I}_\alpha-\frac{\mathbf{s}_k\cdot\mathbf{I}_\alpha}{r_{k\alpha}^3}+\frac{3(\mathbf{s}_k\cdot\mathbf{r}_{k\alpha})(\mathbf{I}_\alpha\cdot\mathbf{r}_{k\alpha})}{r_{k\alpha}^5}\right\}.$$

The first term corresponds to a contact term and the last ones to a dipolar interaction. On the basis of the molecular orbitals of the octahedral complex $[NiF_6]^{4-}$: $|\Psi\rangle=\{D_i(k)\}$, where $D_i(k)$ are the antibonding molecular orbitals occupied by the unpaired electrons[26,27] the superhyperfine (shf) Hamiltonian is $\tilde{H}_{\rm shf}(\alpha)=\langle\Psi|H_{\rm shf}(\alpha)|\Psi\rangle=\mathbf{S}\cdot A^\alpha\cdot\mathbf{I}_\alpha$ (Ref. 28) with $\mathbf{s}_k=\mathbf{S}/2S$ and $H_{\rm shf}(\alpha)=\Sigma_k H(\mathbf{s}_k\cdot\mathbf{I}_\alpha)$. In axial symmetry, with six equivalent α fluorine ions, the superhyperfine interaction spin Hamiltonian is

$$\tilde{H}_{\rm shf}=\sum_{\alpha=1}^{6}\left[A_\parallel S_Z I_Z^\alpha+A_\perp(S_X I_X^\alpha+S_Y I_Y^\alpha)\right],$$

where $A_\parallel=A_{\rm iso}+2A_p$ and $A_\perp=A_{\rm iso}-A_p$, are the components of the shf tensor in axial symmetry.[29]

The experimental results are often expressed in terms of the fraction *f* of unpaired electron spin transferred to an orbit or a F^- ligand. For *d* orbitals that are occupied these fractions are f_s, f_π, f_σ.[30]

The isotropic contribution $A_{\rm iso}$ is due to the contact interaction between the *s* orbitals of fluorine and the d_σ (e_g) electrons of nickel and is equal to $A_{\rm iso}\cong A_s=7600f_s$.[29] The anisotropic term, which is related to the dipolar interaction between the spins of the unpaired electrons of the nickel and the nuclear spin of the fluorine, is equal to $A_p=A_d+(A_\sigma-A_\pi)$. Here, A_d is the classical dipolar interaction, $A_d=(24.8/R^3)\times10^{-4}$ cm^{-1} (*R* is the Ni-F distance in angstroms).[29] Also, A_σ is the shf interaction due to the transfer from e_g symmetry *d* orbitals of nickel to $2p_\sigma$ orbital of fluorine. The e_g electrons transfer to $2p_\sigma$ and experience the nuclear spin; they also participate to the covalent bonding. $A_\sigma=1074.3f_\sigma/5S$.[29] Finally, A_π is the same interaction with

TABLE I. Values of crystal-field strength *Dq*, transferred spin density f_σ, and *k* factor for Ni^{2+} ions in various fluoride perovskites versus their metal-F distance.

	$CsCdF_3$ (Ref. 32)	$KZnF_3$ (Refs. 27, 33)	$BaLiF_3$ (Ref. 21)	$KMgF_3$ (Ref. 34)
Metal-F (Å)	2.281	2.026	2.000	1.987
Dq Ni^{2+} (cm^{-1})	610	736	840	780
f_σ (%)	4.66	4.48	6.14	4.76
k	0.93	0.915	0.881	0.937

t_{2g} orbitals. This transfer is impossible in the case of the Ni^{2+} ion due to the presence of six electrons on these orbitals, and then $A_\pi = 0$.

Then we use the following formulas to estimate the covalency from the parameters of the superhyperfine structure, $A_\parallel = 73.1\times10^{-4}$ cm^{-1} and $A_\perp = 24.2\times10^{-4}$ cm^{-1} for the transition $\Delta M_S = 1$ at $g = 2.235$ in Ni^{2+}-doped $BaLiF_3$:[11,21]

$$A_S = \frac{A_\parallel + 2A_\perp}{3},$$

$$A_p = \frac{A_\parallel - A_\perp}{3}, \quad A_d = \frac{24.8}{R^3}10^{-4}, \quad A_\sigma = A_p - A_d,$$

$$f_s = \frac{A_s}{7600}, \quad f_\sigma = \frac{5A_\sigma}{1074.3},$$

where the f_σ relation is from Ref. 29.

We compare these results with the correction of the Landé factor *g* from the value for the free electron, i.e., 2.0023. To calculate this correction, we use the value of crystal-field parameter $10Dq$ measured by optical absorption and the value of *g* measured by ESR. We have $g = g_e - 8k^2\lambda/10Dq$ with $\lambda_{Ni} = -315$ cm^{-1}. We obtain the *k* normalization factor, which is equal to 1 without any transfer:[31]

$$k^2 = -\frac{(g - g_e)}{8\lambda}10Dq.$$

In Table I, we report the values of the crystal-field strength *Dq*, the transferred spin density f_σ, and the *k* factor for Ni^{2+} ions in various fluoride perovskites versus their metal-F distance which is a good estimate of the Ni-F distance. Three compounds have the classical perovskite structure ($CsCdF_3$, $KZnF_3$, $KMgF_3$), while $BaLiF_3$ has the inverted structure, as previously mentioned. The strongest f_σ transfer, about 6%, is calculated for $BaLiF_3$. This value is consistent with the *k* factor obtained, the farthest from 1 in this case. This strongest covalent character must be related to the inverted structure of $BaLiF_3$. The Ni^{2+} ion is located at the center of a fluorine octahedron whose size is almost identical in $KZnF_3$, $BaLiF_3$, and $KMgF_3$. The main difference lies in the second-nearest neighbors: highly polarizable (1.69×10^{-4} cm^3) divalent barium for $BaLiF_3$ and weakly polarizable (1×10^{-4} cm^3) monovalent potassium in the case of $KMgF_3$ and $KZnF_3$.

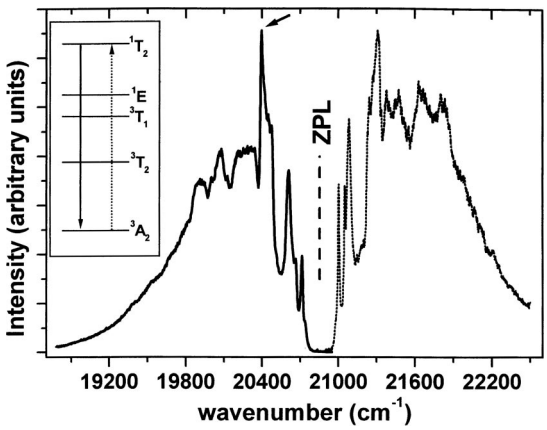

FIG. 1. $^1T_2 \rightarrow {}^3A_2$ emission spectrum of Ni^{2+}-doped $KMgF_3$ (1 mol %) obtained at 21 K under 457.9 nm excitation (solid line). Associated excitation spectrum of Ni^{2+}-doped $KMgF_3$, $^3A_2 \rightarrow {}^1T_2$ recorded at 18 K with the emission fixed at 20 404 cm^{-1} marked by an arrow (dotted line). Dashed line indicates the ZPL position.

The crystal-field strength is also stronger, +8%, in $BaLiF_3$ compared to $KMgF_3$, which has the most similar metal-fluorine distance. This result is consistent with the point-charge model calculations, which give a stronger amplitude (9%) of the electrostatic potential at the center of the inverted perovskite than in a normal perovskite of identical lattice parameter, taking into account the contribution up to the third-nearest neighbors.[35]

IV. OPTICAL MEASUREMENTS

A. Linearity of the coupling in Ni^{2+}:$KMgF_3$

Fig. 1 shows the green emission spectrum of Ni^{2+}-doped $KMgF_3$ obtained at 21 K after excitation at 21 837 cm^{-1} (457.9 nm). This vibronic emission lies between 18 500 and 20 900 cm^{-1} and is associated with the emission from the $^1T_2$ level down to the $^3A_2$ ground level of Ni^{2+}. The purely electronic transition is spin forbidden but allowed by the magnetic dipolar mechanism. The nature of the vibronic sideband can differ from the zero-phonon line (ZPL) due to phonon-induced symmetry modification of the default site.[36,37] In the same figure, the associated excitation spectrum, $^3A_2 \rightarrow {}^1T_2$, is given. It has been recorded at 18 K with the emission fixed at 20 404 cm^{-1}, which corresponds to the position of the most intense line of the emission spectrum. The intensity of the dye laser is nearly independent of the wavelength between 21 000 and 22 500 cm^{-1} and is then assumed to negligibly affect the shape of the spectrum. These two spectra never overlap and then no ZPL was observed. A unique ZPL was expected, due to the existence of only one spin-orbit component for both the $^1T_2$ and $^3A_2$ levels. Using symmetry considerations between the features of the two spectra, the position of the $^1T_2$ electronic level is estimated at the median position 20 852.5 cm^{-1}. A dashed line, plotted in Fig. 1, represents this ZPL position.

In Fig. 2, the excitation spectrum is folded symmetrically around the position of the estimated ZPL to compare the shape of the two spectra according to the following formula:

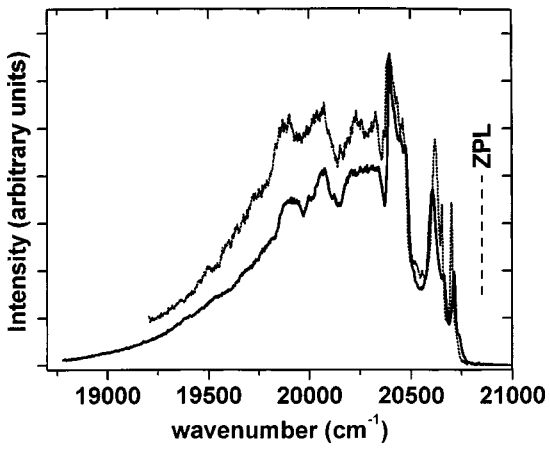

FIG. 2. Emission (solid line) and excitation (dotted line) spectra of the $^3A_2 \leftrightarrow {}^1T_2$ transition of Ni^{2+}-doped $KMgF_3$ presented in Fig. 1. The excitation spectrum has been folded symmetrically around the position of the calculated ZPL (dashed line).

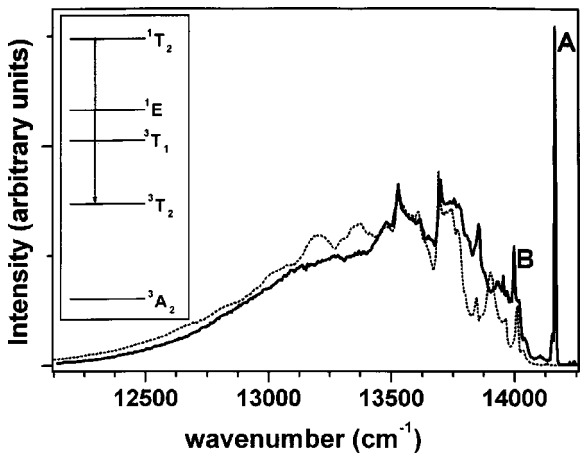

FIG. 3. $^1T_2 \rightarrow {}^3T_2$ emission spectrum of Ni^{2+}-doped $KMgF_3$ obtained at 15 K under 21 837 cm^{-1} excitation (solid line). The zero-phonon lines are labeled *A* and *B*. Simulation of the $^1T_2 \rightarrow {}^3T_2$ emission associated with the two ZPL *A* and *B* calculated with the band shape of the $^1T_2 \rightarrow {}^3A_2$ emission (dotted line).

$x_{\text{folded}} = x_{\text{ZPL}} - (x - x_{\text{ZPL}}) = 2x_{\text{ZPL}} - x$, where x is the abscissa of the excitation spectrum, x_{folded} its abscissa after the symmetry operation, and $x_{\text{ZPL}} = 20\,852.5\ \text{cm}^{-1}$. After this symmetry transformation, the excitation spectrum appears remarkably similar to the emission spectrum with only minor variations in the relative intensities of the lines. The main features are peaking at the same energy shift from the ZPL position. The phonon spectra associated with the $^1T_2$ excited state and $^3A_2$ ground state are then very similar, indicating a mainly linear *e*-ph coupling. The strength of the *e*-ph coupling is also rather identical in the emission and absorption between these two levels, as shown by their great similarity. The same observations have been made with Ni^{2+}-doped $BaLiF_3$.

The main interest of the $^1T_2 \rightarrow {}^3A_2$ transition is the existence of only one spin-orbit component in the two involved electronic states. In such a case, a clear electronic process involving only one initial and one final electronic level takes place in absorption as well as in emission. In many other cases of electronic transitions, the vibronic spectrum can result from the superposition of the phonon spectra associated with the different spin-orbit sublevels. The vibronic spectrum could be different despite identical phonons due to a different spin-orbit splitting in the two electronic states. For instance, the $^3T_2$ level splits into four components under the spin-orbit interaction. They are labeled A_2, T_2, T_1, and E.

Figure 3 shows the red emission spectrum of Ni^{2+}-doped $KMgF_3$ obtained at 15 K under excitation at 21 837 cm^{-1}. This vibronic spectrum is associated with the emission from the $^1T_2$ state down to the $^3T_2$ excited state of Ni^{2+}. The purely electronic transition is spin forbidden but allowed by the magnetic dipolar mechanism. Two ZPL's called *A* and *B* and peaking, respectively, at 13 999 and 14 164 cm^{-1} have been observed as previously mentioned.[36] By using the position of the $^1T_2$ level previously determined at 20 852.5 cm^{-1} and the position of the ZPL's *A* and *B*, we can deduce that the two lowest spin-orbit components E and T_1 of the $^3T_2$ level are lying at 6688 and 6853 cm^{-1}, respectively. No ZPL due to the remaining T_2 and A_2 spin-orbit components of $^3T_2$ appears on the spectrum. The observation of the two spin-forbidden ZPL's in the $^1T_2 \rightarrow {}^3T_2$ emission when it was not observed in the $^1T_2 \rightarrow {}^3A_2$ transition should be attributed to the splitting due to spin-orbit coupling affecting the $^3T_2$ level but not the $^1T_2$ and $^3A_2$ levels.

In Fig. 3, a simulation of the $^1T_2 \rightarrow {}^3T_2$ red emission associated with the two ZPL's *A* and *B* is superimposed, as a dotted line, with the profile of the $^1T_2 \rightarrow {}^3A_2$ green emission duplicated by the following formula:

$$I_R(\omega) = g_A I_G(\omega - \Delta\omega_A) + g_B I_G(\omega - \Delta\omega_B),$$

where $I_G(\omega)$ is the profile of the green emission, $I_R(\omega)$ is the red emission, $\Delta\omega_A$ and $\Delta\omega_B$ are the energy gap between the spin-orbit components of the $^3T_2$ level and the $^3A_2$ level, and Δ_{AB} is the energy difference between the two ZPL's *A* and *B*. The relative intensities associated with the *A* and *B* ZPL's, $g_A = 2g_B$, have been chosen to get the best agreement between the intensity of the most intense phonon replicas lying at 13 526 and 13 961 cm^{-1} of the two spectra, I_R and I_G. The two ZPL's *A* and *B* could not be calculated due to the lack of ZPL's in the $^1T_2 \rightarrow {}^3A_2$ emission spectrum. Whereas the calculation does not give a complete account of all the features, the general shape, the main and strong features, for instance, at 13 526 and 13 691 cm^{-1}, and the global width are correctly reproduced. The rather good agreement in the transposition of the profile from one emission to one another corroborates the purely linear *e*-ph coupling previously observed for the vibronic transitions of Ni^{2+} in $KMgF_3$. Indeed, the phonon spectrum involved in the $^1T_2 \rightarrow {}^3T_2$ emission is associated with the final $^3T_2$ level instead of the $^3A_2$ level in the green emission. Moreover, this simulation of the red vibronic emission indicates that the strength of the *e*-ph coupling involved in the green and red emissions is rather similar.

This same $^1T_2 \rightarrow {}^3T_2$ emission in Ni^{2+}-doped $KMgF_3$ has been recorded with a spectral resolution better than 2 cm^{-1} versus the temperature from 10 to 200 K [Fig. 4(a)]. The

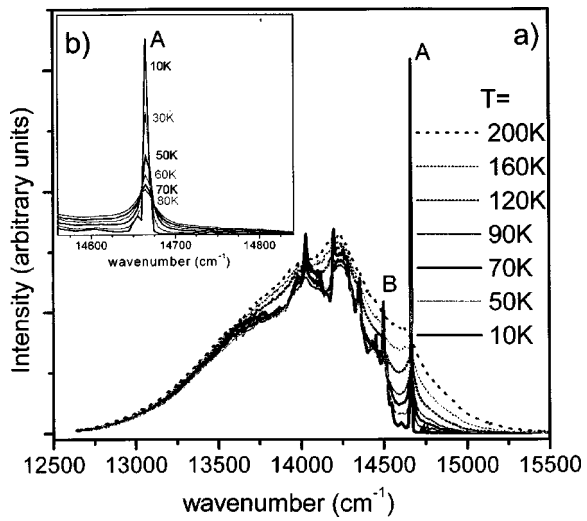

FIG. 4. (a) $^1T_2 \rightarrow {}^3T_2$ emission spectrum of Ni^{2+}-doped $KMgF_3$ vs temperature. (b) Magnification of the section around the ZPL labeled *A* of the $^1T_2 \rightarrow {}^3T_2$ emission spectrum of Ni^{2+}-doped $KMgF_3$ versus the temperature.

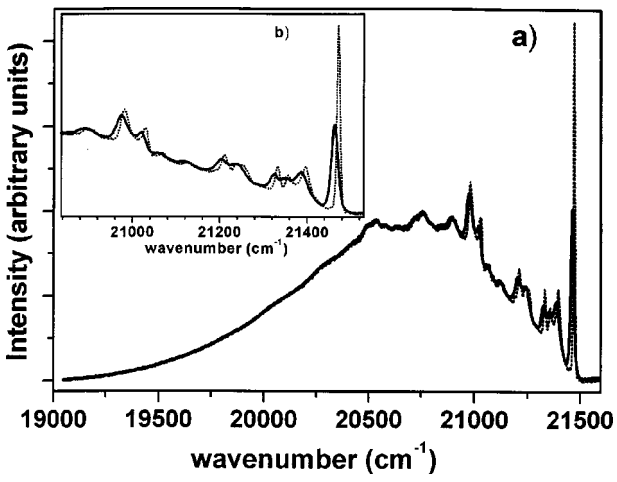

FIG. 5. (a) Emission spectra of the $^1T_2 \rightarrow {}^3A_2$ transition obtained under 21 837 cm^{-1} excitation at 15 K, for Ni^{2+}-doped $BaLiF_3$: solid line, 0.5% of Ni^{2+}; dotted line, 6% of Ni^{2+}. (b) Magnification of the high-energy section of the spectra. Ni^{2+}-doped $BaLiF_3$, 0.5% (solid line) and 6% (dotted line).

entire vibronic band appears at the same central position when the temperature is increased despite a thermal broadening. The value of the first moment of the vibronic spectrum was calculated in order to give a quantitative estimate of the thermally induced shift.[38] At 10 K, $M_{1em}=13\,920 \pm 20\ cm^{-1}$ and at 200 K, $M_{1em}=14\,040 \pm 20\ cm^{-1}$. The thermal shift, 120 cm^{-1}, is mainly induced by the growth of the anti-Stokes component appearing on the high-energy side of the ZPL when the temperature is increased. This thermal shift does not reflect any shift of the overall spectrum as observed in Fig. 4(a). The two ZPL's labeled *A* and *B* are not shifted when the temperature is increased from 10 to 80 K. A magnification of the spectral zone around the ZPL labeled *A* is given in Fig. 4(b). For temperatures higher than 80 K, the ZPL's are homogeneously broadened and difficult to locate with high precision. With quadratic *e*-ph coupling, the thermal shift of the ZPL and the thermal broadening of the ZPL are of the same order of magnitude.[15] Also according to Marco de Lucas, Rodriguez, and Moreno,[38] quadratic *e*-ph coupling induces a thermal shift of the emission and excitation spectra. When we observe the thermal broadening of the ZPL and vibronic sideband, no thermal shift is observed. These thermal observations are still in agreement with our previous statements concerning the pure linearity of the *e*-ph coupling.

B. Concentration dependence on the *e*-ph coupling in Ni^{2+}:$BaLiF_3$

Figures 5(a) and 5(b) report the green emission spectrum associated with the $^1T_2 \rightarrow {}^3A_2$ transition at 15 K in Ni^{2+}-doped $BaLiF_3$ for two different Ni^{2+} concentrations, 0.5 and 6 mol %, in the melt corresponding, respectively, to 0.2% and 1.65% of Li atoms substituted in the crystal. At first, in contrast with Ni^{2+}-doped $KMgF_3$, the spin-forbidden ZP transition is observed for this transition in $BaLiF_3$. When no Ba^{2+} or Li^+ vacancies have been observed in the next-nearest neighbors of Ni^{2+} ions through the transferred hyperfine spectrum caused by an octahedron of six perfectly equivalent F^- ions, the weak distortion of the crystal field due to a long-distance charge compensation and observed as the $\Delta M_S=2$ ESR transition at $g=4.47$ should allow the zero-phonon transition.[11,21] AT 21 K, in Ni^{2+}-doped $KMgF_3$, the lifetime of the $^1T_2$ level is equal to $275 \pm 20\ \mu s$. At 18 K, in $BaLiF_3$ doped with 0.5% Ni^{2+} in the melt, this same level reveals a lifetime of $80 \pm 20\ \mu s$. The shortening of the lifetime should also be considered with respect to the weak symmetry distortion in Ni^{2+}-doped $BaLiF_3$.

The profile of the spectrum is conserved when the high-energy features [Fig. 5(b)] are affected by the concentration change. The different lines peaking between 20980 and 21471.8 cm^{-1} (ZPL) have been deconvoluted by Gaussian shapes in order to estimate their width ($\Delta\omega$), area, and frequency (ω). The results are given in Table II. In the highly doped crystal, a similar shift ($\delta\omega$) of the ZPL and vibronic lines towards the lower energy, about 8 cm^{-1}, is observed. The relative shift between the ZPL and the vibronic replicas is conserved, proving that the phonon frequencies remain unaffected by the concentration variation. In this same crystal, which contains the higher doping amount, all the lines are broadened from +20% to +115% but their areas remain weakly affected, less than 15%. Indeed, the high concentration induces an inhomogeneous broadening of the electronic level and then of the ZPL, inducing the broadening of all the phonon replicas lying near the ZPL. Indeed, the replicas, lying in the limit of 600 cm^{-1} from the ZPL, the phonon cutoff frequency of the crystal, are mainly associated with one-phonon processes and remain narrow enough to exhibit the inhomogeneous broadening. Above this limit, the emitted photons result from the interaction with two or more phonons. In the multiphonon process, the features are homogeneously broadened with respect to one-phonon processes and consequently not resolved, and the inhomogeneous

TABLE II. Width, shift between the two concentrations, area, and frequency corresponding to the deconvolution by Gaussian shapes of the different lines in the $^1T_2 \rightarrow {}^3A_2$ emission at 15 K in Ni^{2+}-doped $BaLiF_3$ for two different Ni^{2+} contents, 0.5% and 6%.

ω (cm^{-1}) ± 1 cm^{-1}	0.5 mol %	21 471.8 ZPL	21 395.5	21 358	21 332	21 210.2	21 027.2	21 984
	6 mol %	21 463.6 ZPL	21 387.2	21 350.7	21 324.7	21 204	21 019	20 978
$\delta\omega$ (cm^{-1})		8.2	8.3	7.3	7.3	6.2	8.2	6.0
$\Delta\omega$ (cm^{-1})	0.5 mol %	7.5	28.5	19.4	11.2	18	15.6	21.3
± 0.5 cm^{-1}	6 mol %	16.2	31.8	23.2	18	26.7	21.3	25.5
Area ($\pm 5\%$)	0.5 mol %	30 987	22 350	9577	6702	8129	7356	14 776
(arb. units)	6 mol %	30 721	20 450	8293	6196	9104	7243	13 947

broadening cannot be appreciated. However, it is clear that the general shape remains unaffected by a variation in the strength of the *e*-ph coupling. The intensity of the *e*-ph coupling, mainly represented by the energy extent of the shape and the intensity of the phonon replicas relatively to the intensity of the ZPL, is exactly the same in the weakly and strongly doped $BaLiF_3$ crystals [Fig. 5(a)]. The excitation spectrum associated with this emission is also kept constant with only a weak inhomogeneous broadening observed in the highly doped crystal.

Some previous studies on Ni^{2+}-doped fluoride compounds[7–9] concluded that the strength of the *e*-ph coupling varied with the impurity concentration. But, in these studies, the determination of the Huang-Rhys coupling factor *S* was not direct because it was determined through the behavior of the nonradiative transition rates (W_{NR}) by lifetime measurements versus concentration. Many other processes, excluding *S* variations, can also induce such a change in W_{NR} values[10] and thus shorten the lifetime. So these conclusions[7–9] resulted from misinterpretations. So, we can unambiguously conclude that *e*-ph coupling is not affected by the concentration of impurities in the crystal in the case of Ni^{2+}-doped fluoride perovskites.

C. Calculation of the vibronic band shape and estimation of the Huang-Rhys parameter

A vibronic spectrum arises from transition between coupled electronic and vibrational states. Originating in the dipole radiation, the emitted intensity is

$$I(\omega) = \frac{64\pi^4\omega^4}{3c^3} G(\omega), \tag{1}$$

where the band shape is given by

$$G(\omega) = \sum_{i,f} W_{li,mf} = \sum_{i,f} \left| \langle \varphi_m | - e \sum_{\alpha} \mathbf{r}_\alpha | \varphi_l \rangle \right|^2 |\langle \chi_{mf}(\mathbf{R}) | \chi_{li}(\mathbf{R}) \rangle|^2, \tag{2}$$

we sum on all the final vibrational states averaged on all the initial vibrational states; the electronic states *l* and *m* are fixed following the Franck-Condon principle.[4] Most of the details of the vibronic transitions can be described in the framework of a simple theory using the adiabatic, harmonic, and Condon approximations.

The case of strong coupling has been described initially, in the case of the *F*-center absorption, by a simplified Huang-Rhys model, assuming that all the lattice modes have the same frequency. In this approximation, with a coupling strength equal to *S*, an *r*-phonon process is weighted by the Poisson distribution $P_r = (S^r/r!)e^{-S}$, resulting in a Pekarian curve at low temperatures. This first model is useful as an indication of how the spectrum becomes spread out in the case of strong coupling between the electronic transition and a particular vibration mode, but is too simplified to account for all the features in the general case. Pryce[5] has developed a method for determining the spectral shape function under the less restrictive conditions of a linear coupling with an arbitrary phonon spectrum. The effective lattice Hamiltonians of the two electronic states differ by linear terms only. The vibronic spectrum is the superposition of contributions in which 0,1,...,*r*,… phonons are involved:

$$G(\omega) = e^{-S} \sum_{r=0}^{\infty} \frac{S^r}{r!} B_r(\omega). \tag{3}$$

An *r*-phonon process has a shape $B_r(\omega)$ with $\int B_r(\omega) d\omega = 1$; $B_0(\omega) = \delta(\omega - \nu)$ is the zero-phonon line, and the *r*-phonon shape, $B_r(\omega)$, is the *r*th convolution, $B_r(\omega) = \int B_{r-1}(\omega') B_1(\omega + r - \omega') d\omega'$, of the one-phonon shape $B_1(\omega)$. Whatever this one-phonon shape may be, when *r* increases the *r*th convolution becomes smoother and tends to a Gaussian curve. It is the reason why a simple and featureless Pekarian curve simulates well the vibronic band shapes in the case of strong *e*-ph coupling.

In a perfect crystal, only the phonons of the center of the Brillouin zone can couple with the optical transitions due to the wave-vector conservation rule in one-phonon processes. Actually, the optically active default breaks the translation symmetry and allows coupling of the phonons of the entire zone with the electronic states. The shape of the one-phonon replica then closely reflects the shape of the mode density $\rho(\omega)$.[3] More accurately, we should define the one-

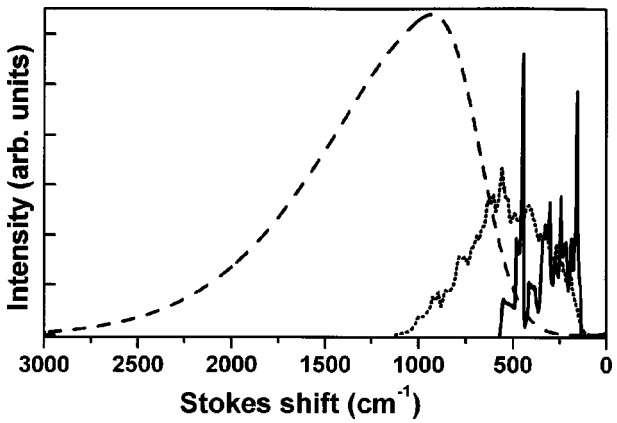

FIG. 6. Contribution of the different orders of the phonon-assisted processes to the vibronic band for a coupling factor $S=3.4$ and the phonon density of states of $BaLiF_3$: one phonon in the solid line, two phonons in the dotted line, and the summation of three- to ten-phonon-assisted processes in the dashed line.

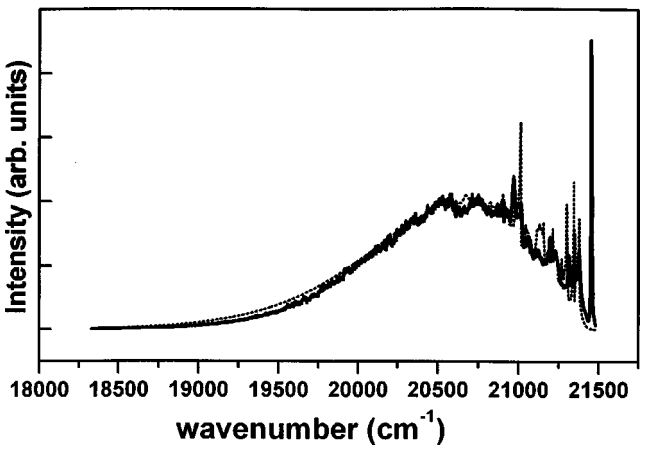

FIG. 7. $^1T_2 \rightarrow {}^3A_2$ emission spectrum of Ni^{2+}-doped $BaLiF_3$ (0.5%) at 10 K. Solid line: experiment at 10 K; dotted line: calculated spectrum with $S=3.4$.

phonon shape $B_1(\omega)$ as being proportional to $S(\omega)\rho(\omega)$. However, as we are not able to estimate the Huang-Rhys factor as a function of the frequency of the lattice modes, we define a unique coupling factor S for the whole vibration spectrum.

The experimental emission band shape is calculated by using the relationships (1) and (3) for $BaLiF_3$ (Fig. 6). The normalized one-phonon density of states is obtained in the lattice dynamics calculations using a rigid ion model.[19,20] The two-phonon shape is the convolution of the one-phonon shape on itself. For $r \geqslant 3$, the band shape is a Gaussian curve of width $\sigma_0\sqrt{r}$, where σ_0 is the half width at half maximum of the Gaussian curve, which would be equivalent to one-phonon processes centered around $r\overline{\omega}$, where $\overline{\omega}$ is the average frequency of the phonon spectrum. In the practical case, we first calculate the two-phonon band shape by self-convolution of the one-phonon density of states, and we then simulate the curve by using a Gaussian shape of width $\sigma_0\sqrt{2}$.[11] In case of intermediate coupling ($S \ll 10$) corresponding to Ni^{2+} ions, the summation is limited to $r=10$ in formula (3).

This model allows the simulation of the contribution arising from all phonons of the matrix measured by neutron scattering in the entire first Brillouin zone[19,20] and not only the optical modes measured in the center of the Brillouin zone by Raman and Brillouin spectroscopies. However, it does not allow one to account for some of the sharpest features that are due to coupling with normal modes associated with the NiF_6 octahedron. To account for these features, we should define an additional density of states consisting of a discrete frequency spectrum of the normal modes. The strength of the coupling with these molecular modes should be different from the coupling with the phonons of the crystal. In the case of Cr^{3+}-doped $KMgF_3$, they give rise to the strongest and sharpest features of the spectrum[25] even though they participate finally for several percent only to the area of the vibronic band that arises mostly from the phonons of the crystal. These normal modes give rise to the strongest replicas when they are lying above the phonon cutoff frequency of the lattice; they are said to be localized because their energy cannot propagate in the lattice. Lying in a gap of the density of states, they are known as gap modes,[1] which are less strongly coupled than the localized modes because they can transfer their energy to the lattice. The weakest replicas arise from resonant normal modes that are lying in the same frequency region as many phonons.

The strength of the *e*-ph coupling, expressed by the value of the Huang-Rhys coupling factor *S*, has been determined in Ni^{2+}-doped $BaLiF_3$ and $KMgF_3$ through simulation of the vibronic band shape using the modified Pryce model previously described and the phonon density of states of each crystal.[19,20] Figure 7 illustrates the rather good agreement between experimental and simulated band shape, for instance, with Ni^{2+}-doped $BaLiF_3$. We have compared the values obtained for the $^1T_2 \rightarrow {}^3A_2$ emission at low temperature: for Ni^{2+}-doped $BaLiF_3$, $S=3.4$ (Fig. 7); for Ni^{2+}-doped $KMgF_3$, $S=2.5$; with the estimation of the covalency of the $[NiF_6]^{4-}$ complex in these two crystals, 6.14% and 4.76% for the f_σ transfer in $BaLiF_3$ and $KMgF_3$, respectively. As previously mentioned by Vink and Meijerink,[12] the *e*-ph coupling is found to increase with the covalency of the host lattice. Due to the Jahn-Teller effect, Mn^{2+}-doped samples seem to behave in the opposite way.[17] An identical value of the Huang-Rhys parameter found for the two Ni^{2+} concentrations in $BaLiF_3$ confirms the lack of influence of the concentration on the coupling.

V. CONCLUSION

A purely linear character of the *e*-ph coupling has been seen in these Ni^{2+}-doped fluoride perovskites through the similarity of different emission and excitation vibronic band shapes, reflecting the phonon frequency spectrum associated with different electronic states. Also, no thermally induced shift of the ZPL or sideband has confirmed this purely linear character.

No concentration dependence of the strength of *e*-ph coupling has been observed in the optical spectra of the studied Ni^{2+}-doped compounds. An inhomogeneous broadening

was, however, clearly observed and should be partially responsible for the variations in the lifetime measurements reported in other works. The increase of the covalent character of the host lattice surrounding the Ni^{2+} ion induces an increase of the strength of the *e*-ph coupling.

ACKNOWLEDGMENTS

P. Goldner is acknowledged for fruitful discussions. N. Gardant is acknowledged for recording some emission spectra.

[1] A. S. Barker and A. J. Sievers, Rev. Mod. Phys. **47**, 1 (1975).
[2] Y. Farge and M. P. Fontana, *Defects in Crystalline Solids: Electronic and Vibrational Properties of Point Defects in Ionic Crystals* (North-Holland, Amsterdam, 1979).
[3] D. Curie, Optical properties of ions in solids, edited by B. Di Bartolo (Plenum, New York, 1975).
[4] Karl K. Rebane, *Impurity Spectra of Solids* (Plenum, New York, 1970).
[5] M. H. L. Pryce, *Phonon in Perfect Lattices with Point Imperfections*, edited by R. W. H. Stevenson (Oliver & Boyd, Edinburgh, 1966).
[6] R. Russi, G. A. Barbosa, M. Rousseau, and J. Y. Gesland, J. Phys. (France) **45**, 1773 (1984).
[7] J. M. Breteau, Ph.D. thesis, University of Paris 6 (1986).
[8] F. Auzel and J. M. Breteau, J. Phys. (France) **48**, C7-451 (1987).
[9] F. Auzel, J. M. Breteau, and D. Meichenin, J. Lumin. **40&41**, 595 (1988).
[10] C. de Mello Donega, A. Meijerinkand, and G. Blasse, J. Lumin. **62**, 189 (1994).
[11] M. Mortier, Ph.D. thesis, University of Paris 6 (1994).
[12] A. P. Vink and A. Meijerink, J. Phys. Chem. Solids **61**, 1717 (2000).
[13] A. P. Vink, M. A. de Bruin, and A. Meijerink, J. Phys.: Condens. Matter **12**, 8607 (2000).
[14] A. P. Vink, M. A. Reijme, and A. Meijerink, J. Lumin. **92**, 189 (2001).
[15] J. Margerie, J. Phys. (France) **26**, 268 (1965).
[16] M. D. Sturge, Solid State Commun. **9**, 899 (1971).
[17] F. Rodriguez, H. Riesen, and H. U. Güdel, J. Lumin. **50**, 101 (1991).
[18] J. Ferguson, H. U. Güdel, E. R. Krausz, and H. J. Guggenheim, Mol. Phys. **28**, 879 (1974).
[19] S. Salaun, M. Mortier, J. Y. Gesland, M. Rousseau, and B. Hennion, J. Phys.: Condens. Matter **5**, 7615 (1993).
[20] A. Boumriche, J. Y. Gesland, A. Bulou, M. Rousseau, J. L. Fourquet, and B. Hennion, Solid State Commun. **91**, 125 (1994).
[21] M. Mortier, J. Y. Gesland, B. Piriou, J. Y. Buzaré, and M. Rousseau, Opt. Mater. **4**, 115 (1994).
[22] B. Di Bartolo, *Optical Interactions in Solids* (Wiley, New York, 1967).
[23] M. Mortier, J. Y. Gesland, and M. Rousseau, Solid State Commun. **89**, 369 (1994).
[24] M. Mortier, J. Y. Gesland, M. Rousseau, F. Auzel, and D. Meichenin, C.R. Acad. Sci. Paris, t.322, Série Iib, 233 (1996).
[25] M. Mortier, Q. Wang, J. Y. Buzaré, M. Rousseau, and B. Piriou, Phys. Rev. B **56**, 3022 (1997).
[26] R. G. Shulmann and S. Sugano, Phys. Rev. **130**, 506 (1963).
[27] J. Y. Buzaré, Ph.D. thesis, University of Caen, France (1974).
[28] A. Abragam and M. H. L. Pryce, Proc. R. Soc. London, Ser. A **205**, 135 (1951).
[29] A. Abragam and B. Bleaney, *Résonance Paramagnétique Électronique des Ions de Transition* (Presses Universitaires de France, Paris, 1971).
[30] J. Owen and J. H. M. Thorney, Rep. Prog. Phys. **29**, 675 (1966).
[31] J. E. Wertz and J. R. Bolton, *Electron-Spin Resonance* (McGraw-Hill, New York, 1972).
[32] B. Villacampa, R. Cases, V. M. Orera, and R. Alcala, J. Phys. Chem. Solids **55**, 263 (1994).
[33] J. Y. Buzaré and J. C. Fayet, C.R. Acad. Sc. Paris, **279**, B353 (1974).
[34] T. P. P. Hall, W. Hayes, R. W. H. Stevenson, and J. Wilkens, J. Chem. Phys. **38**, 1977 (1963).
[35] T. Yosida, H. Aoki, H. Takeuchi, M. Arakawa, and K. Horai, J. Phys. Soc. Jpn. **46**, 1661 (1979).
[36] W. E. Vehse, K. H. Lee, S. I. Yun, and W. A. Sibley, J. Lumin. **10**, 149 (1975).
[37] W. V. Iverson and W. A. Sibley, J. Lumin. **20**, 311 (1979).
[38] M. C. Marco de Lucas, F. Rodriguez, and M. Moreno, J. Phys.: Condens. Matter **7**, 7535 (1995).